THE JOURNAL OF CHEMICAL PHYSICS **123**, 154904 (2005)

The polymerization of actin: Structural changes from small-angle neutron scattering

Alexander I. Norman[a]
Department of Chemistry and Biochemistry and Department of Chemical and Biomolecular Engineering, The University of Maryland College Park, College Park, Maryland 20742

Robert Ivkov
Triton BioSystems, Inc., Chelmsford, Massachusetts 01824

Jeffrey G. Forbes
Proteomics and Nanotechnology Section, Laboratory of Muscle Biology, National Institute of Arthritis and Musculoskeletal and Skin Diseases (NIAMS), National Institutes of Health (NIH), Department of Health and Human Services (DHHS), Building 50, Bethesda, Maryland 20892

Sandra C. Greer[b]
Department of Chemistry and Biochemistry and Department of Chemical and Biomolecular Engineering, The University of Maryland College Park, College Park, Maryland 20742

(Received 23 February 2005; accepted 22 July 2005; published online 19 October 2005)

We present a new analysis of small-angle neutron-scattering data from rabbit muscle actin in the course of the polymerization from *G*-actin to *F*-actin as a function of temperature. The data, from Ivkov *et al.* [J. Chem. Phys. **108**, 5599 (1998)], were taken in D_2O buffer with Ca^{2+} as the divalent cation on the *G*-actin in the presence of ATP and with KCl as the initiating salt. The new analysis of the data using modeling and the method of generalized indirect fourier transform (O. Glatter, GIFT, University of Graz, Austria, http://physchem.kfunigraz.ac.at/sm/) provide shapes and dimensions of the *G*-actin monomer and of the growing actin oligomer in solution as a function of temperature and salt concentration. This analysis indicates that the *G*-actin monomer, under the conditions given above, is a sphere 50–54 Å in diameter as opposed to the oblate ellipsoid seen by x-ray crystallography. The *F*-actin dimensions are consistent with x-ray crystal structure determinations. © *2005 American Institute of Physics*. [DOI: 10.1063/1.2039088]

I. INTRODUCTION

The globular protein *G*-actin polymerizes under certain conditions (such as temperature, actin concentration, and salt concentration) to form the filamentary protein aggregate *F*-actin.[1–3] *G*-actin consists of 375 amino acid residues with a total molecular weight of 42 000 Da. A molecule of adenosine triphosphate (ATP) or adenosine diphosphate (ADP) and a divalent cation are associated with each *G*-actin molecule. X-ray studies of crystalline ATP actin complexed to DNase I,[4] or complexed to gelsolin,[5,6] or complexed to latrunculin[7] or uncomplexed[8] are all "virtually identical"[9] and indicate that the *G*-actin molecule is roughly an oblate ellipsoid with dimensions of 55 × 55 × 35 Å. *F*-actin is a double-stranded right-handed helix with a maximum diameter of 90–95 Å,[10–13] a crossover distance of 360–400 Å, which gives a helical turn of 720–800 Å,[2] and lengths of up to several microns.[14] *F*-actin has roles in maintaining cell shape and in constructing the contractile fibers of muscle cells.[2] The assembly and disassembly of actin are utilized by cells for movement.[15–19]

The mechanism of actin polymerization[20–24] proceeds via monomer activation to form dimers,[25,26] which, in turn, react with monomers to form trimers. Monomeric activation is believed to be due to a conformational change in the actin monomer through ion binding with an initiating salt, e.g., KCl.[20] The trimers are thought to be the nuclei for further polymerization of the actin.

In 1998, Ivkov *et al.*[27] reported small-angle neutron-scattering (SANS) measurements from solutions of rabbit muscle *G*-actin at 3.00 mg/ml in D_2O buffer with varying concentrations of KCl. SANS measurements were recorded at temperatures between 0 and 25 °C, in increments of 2 °C. The SANS intensity $I(q)$ at a given q value (where the scattering vector $q=4\pi \sin \theta/\lambda, 2\theta$ being the scattering angle and λ the wavelength of the incident radiation) showed a striking increase in the temperature range of the polymerization. The transition was shown to be sharper for lower concentrations of KCl. The observations for rabbit muscle actin are analogous to SANS observations on the polymerization of α-methylstyrene.[28]

In 2001–2003, the extent of polymerization ϕ, the fraction of monomer converted to polymer, was measured as a function of temperature by Niranjan and co-workers[29,30] using fluorescence spectroscopy and was shown to exhibit a maximum, indicating the onset of a net depolymerization at higher temperatures. This behavior, reminiscent of the behavior of the viscosity during the polymerization of sulfur,[31] was interpreted in terms of a Flory-Huggins-type lattice model.

---

[a] Electronic mail: anorman1@umd.edu
[b] Electronic mail: sgreer@umd.edu

Our efforts in this paper are to reanalyze the SANS data collected by Ivkov *et al.*[27] in the context of the new information on $\phi(T)$ and with a new method for the analysis of the SANS data. We extract $\phi(T)$ from the SANS data, we examine the low-q scaling behavior for information on the actin shape, and we fit available models to the SANS data to extract information regarding particle dimension and degree of polymerization. We then perform an inverse Fourier transform on the SANS data to extract the pair distance distribution function $p(r)$. This calculation allows data in the 10–1000-Å size range to be viewed with high resolution in real space. Particle shape and size and size distributions are thus determined.

II. EXPERIMENT

A. Sample preparation

The details of the isolation and purification of actin from rabbit muscle have been documented by Ivkov *et al.*[27] and the reader is referred there and to the references therein. The actin was prepared in the presence of ATP with Ca^{2+} as the divalent counterion and with KCl as the initiating salt. The actin was in D_2O buffer in order to reduce incoherent neutron scattering and provide contrast with the hydrogens on the actin molecules. An actin concentration of 3.00 mg/ml was used at three different concentrations of KCl: 5.4±0.5, 8.9±0.8, and 15±1 mM.

B. Instrumentation

The SANS experiments were conducted at the National Institute for Standards and Technology Center for Neutron Research (NCNR), Gaithersburg, MD on the 30-m SANS instrument (NG3).[32] Two instrumental settings were used to achieve a broad q range: a 2-m sample-to-detector distance ($0.024 \leqslant q \leqslant 0.31$ Å^{-1}) and a 8-m sample-to-detector distance ($0.008 \leqslant q \leqslant 0.31$ Å^{-1}), where the scattering vector $q = 4\pi \sin\theta/\lambda$. The average neutron wavelength λ, set by a mechanical velocity selector, was 6 Å with $\Delta\lambda/\lambda = 15\%$.

The samples were loaded into either 1- or 5-mm quartz cells and mounted in a temperature-controlled seven-position sample changer. The temperature of the sample changer was controlled via circulating liquid and was measured to be 0.1 °C with a thermocouple in the middle of the sample position where the neutron beam passed through.

C. Data reduction

The original raw SANS data have been completely reanalyzed. The scattered intensity was corrected for dark background and empty cell scattering via a subtraction from each data set. The spectra were also corrected for detector response variations, which takes into account any nonlinearity of the detector. The corrected intensities were placed on an absolute scale using (a) a silica standard for the data collected using the 8-m sample-to-detector configuration and (b) a 1-mm path length water standard for the 2-m data. Due to time constraints in the beam time available, not all samples were investigated using both configurations. The beam center and edge effects of the detector were masked from the data. The two-dimensional data sets were then radially averaged to obtain one-dimensional $I(q)$ vs q data sets. Finally, the low-level incoherent background scattering was estimated[33] from the asymptotic slopes of $I(q)q^4$ vs q^4 and subtracted from the data.

The uncertainties associated with the SANS experiments are dependent on various factors such as the detector count rate, the estimation in conversion of pixel number to scattering vector, and the secondary standard. Such errors were calculated and written into the output files created from the software at the NCNR.

The reduced SANS data are available through the Electronic Physics Auxiliary Publication Service.[34]

III. THEORY AND DATA ANALYSIS

A SANS spectrum can be understood by concentrating on three specific regions of the curve. At very low values of q ($qR_g \leqslant 1$, where R_g is the radius of gyration of the scattering particle), the behavior of $I(q)$ is independent of particle shape. This is because the spatial resolution is not sufficient to elucidate particle shape and only information regarding dimension can be obtained. In this case $I(q)$ is described by the Guinier relation:[35]

$$I(q) = I(0)\exp\{-q^2R_g^2/3\}, \tag{1}$$

where R_g is the radius of gyration of the particle and $I(0)$ is the scattered intensity at $q=0$, which can be obtained from a double logarithm plot:

$$\ln[I(q)] = \ln[I(0)] - \frac{q^2R_g^2}{3}. \tag{2}$$

In the high-q region of the scattering curve, the spatial resolution is high enough to distinguish the interface between the particle and the solvent, and $I(q)$ typically scales as q^{-4}, known as Porod's law.[36]

The intermediate range of $I(q)$ is the region from which information regarding particle size and shape can be extracted.[37,38] In this region, power-law scattering results and $I(q)$ scales as q^{n-3}, where n is the dimensionality of the scattering species. For example, the scattered intensity of a rod ($n=2$) scales as q^{-1}. Similarly, spherical objects will scale as q^0 and flexible chains or lamellar structures will scale as q^{-2} in this region.

The SANS group at NCNR provides modeling routines that are user friendly and statistically robust.[39] A variety of models are available for the form factor $P(q)$ that describes the scattering due to the shape of the scattering particles and for the structure factor $S(q)$ that describes the scattering due to the interactions between the particles. Then the total scattering $I(q) = \phi V_{\mathrm{part}} P(q) S(q)$, where ϕ is the volume fraction of the particles and V_{part} is the volume of a particle.[36] For our purposes, three of these models will be discussed. The first model, the simplest case, is $P(q)$ from noninteracting hard monodisperse spheres.[40]

$$P(q) = \left\{ \frac{3[\sin(qR) - qR\cos(qR)]}{(qR)^3} \right\}^2, \tag{3}$$

where R is the radius of the sphere. However, no such system is perfectly monodisperse which results in the damping of the oscillations in $P(q)$. Hence, a model describing the scattering from a polydisperse array of spheres is available from the NCNR website.[39] This model calculates the scattered intensity for a population of polydisperse spheres with hard-sphere interactions between the particles. A Schulz distribution[39] is used to describe the polydispersity p of the diameters of the spheres, where $p=s/R$, where s^2 is the variance of the distribution and R is the mean particle radius. The hard-sphere interactions are described by the structure factor $S(q)$:[41]

$$S(q) = 1 + 4\pi \frac{N}{V} \int_0^\infty [g(r) - 1] r^2 \frac{\sin(qr)}{qr} dr, \tag{4}$$

where N is the number of particles in a volume V at a distance r from any given particle. The radial distribution function $g(r)$ is taken from the Percus-Yevick approach.[42]

The second model is that of an ellipsoid as the scattering particle. A prolate ellipsoid is needlelike in shape as opposed to an oblate ellipsoid, which is disklike and has a very different scattering profile. For the prolate ellipsoid,[39]

$$P(q) = \int_0^1 f^2[qr_b\{1 + x^2(\nu^2 - 1)\}^{1/2}]dx, \tag{5}$$

$$f(z) = 3V_{\mathrm{ell}} \frac{(\sin z - z\cos z)}{z^3}, \tag{6}$$

$$V_{\mathrm{ell}} = \left(\frac{4}{3}\right) \pi r_a r_b^2, \quad \nu = \frac{r_a}{r_b}, \tag{7}$$

where $f(z)$ is the scattering amplitude and $z=qr_b\{1+x^2(\nu^2-1)\}^{1/2}$, r_a is the short axis of the ellipsoid, r_b is the long axis, ν is the ratio of the short axis to the long axis, $x=R_g^2 q^2$, and V_{ell} is the volume of the ellipsoid. The same model is used for an oblate ellipsoid. In this NCNR model, the $S(q)=1$ and no interparticle interactions are taken into account.

Finally, a cylindrical model for the scattering particles is fitted to the data for the polymeric actin. The cylinder is assumed to be circular in cross section and monodisperse:[36]

$$P(q) = \int_0^{\pi/2} \left[\frac{2J_1(qR\sin\alpha)}{(qR\sin\alpha)} \times \frac{\sin\{qL\cos(\alpha/2)\}}{\{qL\cos(\alpha/2)\}} \right]^2 \sin\alpha d\alpha, \tag{8}$$

where J_1 is a first-order Bessel function, R is the radius of the circular cross section, L is the cylinder length, and α is the angle between the cylinder axis and the scattering vector q. In this model, again the $S(q)=1$ and no interparticle interactions are taken into account.

The last method of data analysis involves the Fourier transformation of the scattering data. The conventional Fourier transformation of $I(q)$ involves the integral[43]

$$p(r) = \frac{1}{2\pi^2} \int_0^\infty I(q) qr \sin(qr) dq, \tag{9}$$

which yields the pair distance distribution function $p(r)$, where r is the distance in real space. This function can be used to determine the size, shape, and internal structure of scattered particles with high accuracy in the size range of 10–1000 Å. The $p(r)$ function can be understood as follows. The scattered particle is divided into many small volume elements (small in comparison to local-density fluctuations). The $p(r)$ function is proportional to the product of the different scattering lengths $(n_i n_k)$ of two volume elements i and k with a center-to-center distance between r and $r+dr$. Similarly, the height of the $p(r)$ function is proportional to the number of such scattering lengths that are found inside the particle within the interval r and $r+dr$. The direct calculation of $p(r)$ using Eq. (9) requires scattering data in the full q range from 0 to ∞. A limited q range in a data set will lead to strong oscillations in $p(r)$. These effects have been minimized in a new data analysis technique using the indirect Fourier transformation.[43–48] This method simultaneously performs desmearing and Fourier transformation assuming that $p(r)=0$ for $r > D_{\max}$, where $D_{\max}$ is the maximum length in the scattering particle. If, however, the concentration of particles increases to levels where $S(q)$ becomes relevant in the overall scattered intensity, then transforming $I(q)$ into real space leads to a Fourier transform that can barely be interpreted due to such strong oscillations at larger r values. Consequently, a still more advanced technique has been developed to eliminate interparticle contributions without neglecting part of the scattering profile, which is important in

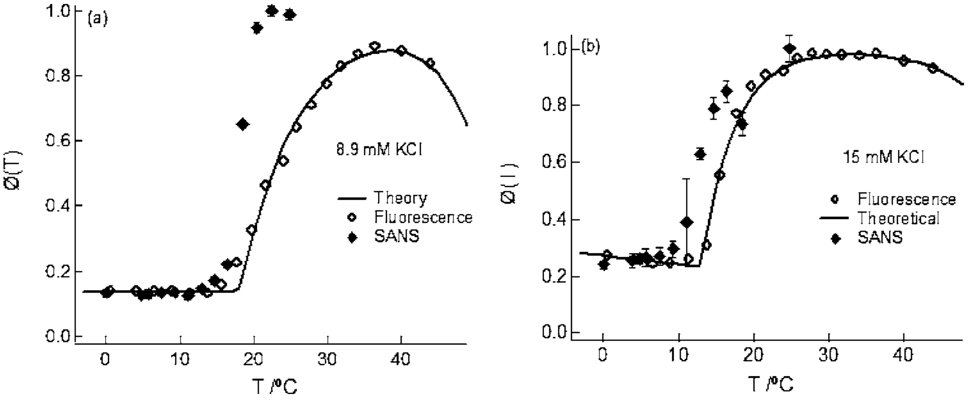

FIG. 1. Extent of polymerization vs temperature for actin at 3.0 mg/ml in D_2O buffer at (a) 8.9-mM KCl and (b) 15-mM KCl. Filled symbols indicate SANS data and open symbols show data from fluorescence measurements taken by Niranjan *et al.* and the solid line is a theoretical fit to the fluorescence measurements (Ref. 30).

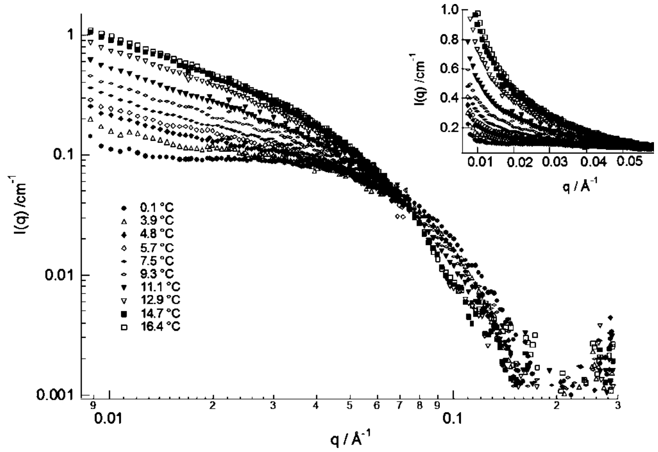

FIG. 2. The SANS intensity $I(q)$ as a function of scattering vector q for 3 mg/ml actin with 15-mM KCl. Error bars have been excluded for clarity. Error bars at low q values (lower than 0.1 Å^{-1}) do not exceed the size of the symbols.

cases of larger structures such as elongated systems.[43,47–49] The correct $p(r)$ can be recovered by separation of the particle interactions during the evaluation process. The technique, termed as the "generalized indirect Fourier transformation" (GIFT),[50] allows for the simultaneous determination of both $P(q)$ and $S(q)$. We apply the GIFT method to the SANS data by using the commercially available PCG software (version 1.01.02).[51]

IV. RESULTS AND DISCUSSION

A. Extent of polymerization

The extent of polymerization of actin $\phi(T)$, the fraction of monomer converted to polymer, can be calculated from the SANS data. This was previously done by Ivkov *et al.*[27] by plotting $I(q)$ at a given q value (q=0.02 Å^{-1}). Here we define $\phi(T)$ as the relative invariant,

$$Q = \int_{q_1}^{q_2} I(q)dq. \tag{10}$$

This is statistically more accurate and more easily determined. The q range used was between 0.014 and 0.07 Å^{-1}. The data were then normalized between 0 and 1 and plotted as a function of temperature. This was done for the actin polymerization at 8.9 and 15-mM KCl; there were insufficient data taken at 5.4-mM KCl. This analysis is shown in Fig. 1 along with the data from Niranjan and co-workers.[29,30] The reproducibility of the polymerization temperatures[29,30] is generally ±2 °C. Given that the experiments were performed on different batches of actin solution by different workers and at different times and using different experimental probes, the data agree remarkably well.

The behavior of $\phi(T)$ indicates the low level of polymerization (dimerization only) at low temperatures, then the dramatic increase in $\phi(T)$ at the polymerization temperature T_p followed by a maximum in $\phi(T)$ and the depolymerization at higher temperatures.

B. Analysis of the SANS data by scaling

Figure 2 shows the scattering data as a function of temperature for the actin samples at 15-mM KCl. The data are presented in double logarithmic form so as to illustrate the differences more clearly; the inset displays the same data in linear form. The inset shows a general increase in scattered intensity as the temperature is increased. The double logarithm plot shows a clear change in slope of $I(q)$ vs q at low q. For example, the scattered intensity scales as q^0 at 0.1 °C,

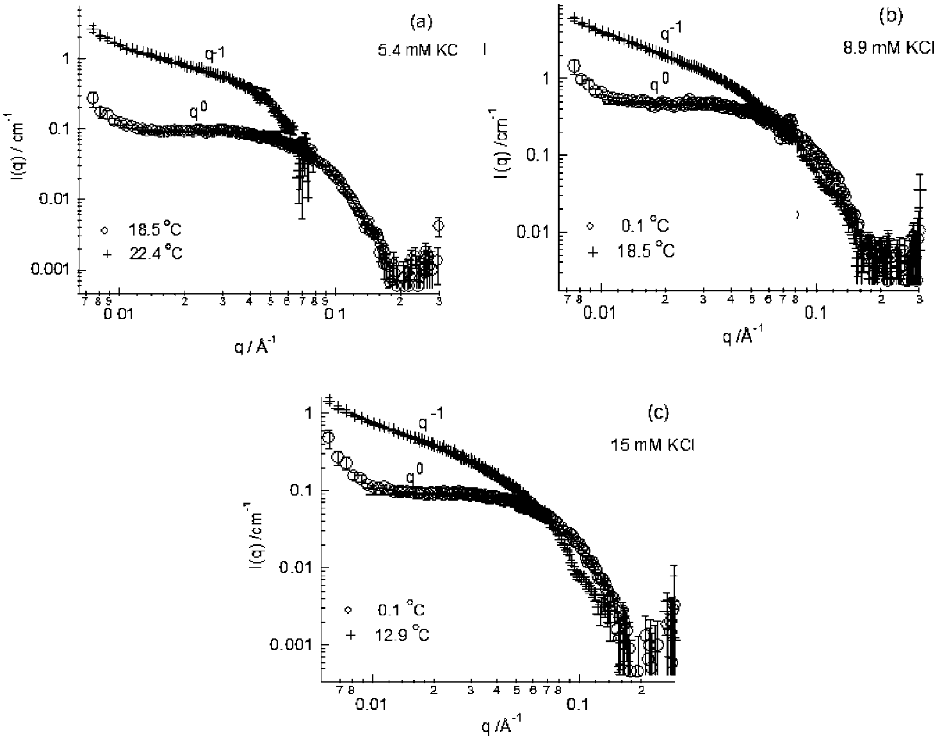

FIG. 3. Scaling of the SANS data for polymerizing actin. (a) Actin with 5.4-mM KCl showing slopes corresponding to spherical (slope=0) and cylindrical forms (slope=−1) of *G*-actin and *F*-actin at 18.5 and 22.4 °C, respectively; (b) actin with 8.9-mM KCl showing slopes corresponding to spherical and cylindrical forms at 0.1 and 18.5 °C, respectively; and (c) actin with 15-mM KCl showing slopes corresponding to spherical and cylindrical forms at 0.1 and 12.9 °C, respectively.

TABLE I. Scaling analysis of the SANS data for the polymerization of *G*-actin to *F*-actin, at all concentrations of KCl and all temperatures, with the predicted shapes determined from the slopes of $I(q)$ at low q. * indicates which data have been analyzed by modeling, as listed in Table II.

[KCl] (mM)	T (°C)	Slope at low q	Shape from scaling	[KCl] (mM)	T (°C)	Slope at low q	Shape from scaling
5.4	4.8	~0	Sphere	8.9	20.4	−1.21	Cylinder*
5.4	5.7	~0	Sphere	8.9	22.4	−1.22	Cylinder
5.4	7.5	~0	Sphere	8.9	24.8	−1.23	Cylinder*
5.4	14.7	~0	Sphere	15	0.1	~0	Sphere*
5.4	18.5	−0.04	Sphere*	15	3.9	−0.42	Ellipsoid*
5.4	20.4	−0.20	Ellipsoid	15	4.8	−0.58	Ellipsoid*
5.4	22.4	−0.48	Ellipsoid	15	5.7	−0.67	Ellipsoid
8.9	0.1	~0	Sphere	15	7.5	−0.74	Ellipsoid
8.9	4.8	−0.13	Ellipsoid*	15	9.3	−0.78	Ellipsoid*
8.9	5.7	−0.37	Ellipsoid	15	11.1	−0.81	Ellipsoid*
8.9	11.1	−0.42	Ellipsoid	15	12.9	−0.97	Cylinder*
8.9	12.9	−0.52	Ellipsoid	15	14.7	−1.07	Cylinder*
8.9	14.7	−0.52	Ellipsoid	15	16.4	−1.14	Cylinder*
8.9	16.4	−0.92	Cylinder	15	18.5	−1.15	Cylinder
8.9	18.5	−1.09	Cylinder*	15	24.8	−1.24	Cylinder*

indicating a spherical particle consistent with *G*-actin. This changes, however, at 3.9 °C where $I(q)$ scales as $\sim q^{-0.5}$. At higher temperatures, this trend continues and the slopes approach unity, suggesting a change in the shapes of the scattering species from spheres to rods. Examples of such plots, illustrating the spherical and cylindrical forms of actin that would correspond to unpolymerized and polymerized actin, are shown in Figs. 3(a)–3(c) at three different KCl concentrations. Note that as the KCl concentration increases, the polymerization temperature for actin is reduced.[27,29,30]

On close inspection of Figs. 2 and 3, some samples (e.g., those at 0.1 °C) show an increase in $I(q)$ at the lowest q values, which is an evidence of slight aggregation of the filaments into larger structures. This is believed to have been caused by the technique used in adding the KCl to the actin solution,[27] in that transient local high concentrations of salt could cause some bundling of actin filaments.[52] These structures are too large to be measured by SANS.

The likely intermediate for the transition between a sphere and a rod is a prolate ellipsoid. The scaling of $I(q)$ at low q and the particle shapes expected from the scaling are shown in Table I. All three data sets show the progression from sphere to prolate ellipsoid to rod as the temperature increases and the polymerization progresses. Thus the scaling analysis gives us a qualitative picture of the structural changes in actin in the course of polymerization.

C. Analysis of the SANS data by modeling

For a more quantitative analysis, we turn to the modeling of the SANS data using the polydisperse hard sphere to model unpolymerized *G*-actin, using the prolate ellipsoid to model the oligomeric intermediate species, and using the rigid cylinder to model polymerized *F*-actin. We tried to model the unpolymerized actin using a NIST NCNR (Ref. 39) model for an oblate ellipsoid, since the monomer structure in crystals has been shown to be of this shape, but the oblate ellipsoid did not fit the data. We tried to model the polymeric actin as a wormlike chain,[39] but this model did not fit the scattering from actin filaments.

Modeling could not be performed on all the SANS data. In order for modeling to be successful (both for the models described here and for the GIFT technique below), the q range must be broad enough and in some situations (when the data were not investigated in both 2- and 8-m SANS configurations), this was not the case. In these situations, we have assumed a structure based on the scaling analysis (see Table I) and on models that succeeded at adjacent temperatures. The results of all the modeling fits are shown in Table II.

Figure 4 shows fits to the two sets of data at temperatures where the actin is not polymerized: (a) the fit of the polydisperse hard sphere and the oblate ellipsoid models for

TABLE II. Parameters from fits to the SANS models and from pair distance function analyses. For sphere models, R is the radius and PD is the polydispersity. For prolate ellipsoid models, R_1 is the short axis and R_2 is the long axis. For cylinder models, R is the radius and L is a length. The uncertainties in R, R_1, R_2, and $D_{\max}$ are ±1 Å; the uncertainty in L is ±10 Å.

[KCl] (mM)	T (°C)	Model	Fit parameters from modeling	Fit parameters from $p(r)$
5.4	18.5	Sphere	R=23 Å, PD=18%	R=27 Å, $D_{\max}$=52 Å
8.9	4.8	Ellipsoid	R_1=22 Å, R_2=38 Å	R=25.5 Å, $D_{\max}$=72 Å
8.9	18.5	Cylinder	R=31 Å, L=500 Å	R=37.5 Å, L=495 Å
8.9	20.4	Cylinder	R=32 Å, L=600 Å	R=42 Å, L=582 Å
8.9	24.8	Cylinder	R=39 Å, L=700 Å	R=42 Å, L=682 Å
15	0.1	Sphere	R=25 Å, PD=18%	R=25.2 Å, $D_{\max}$=60 Å
15	3.9	Ellipsoid	R_1=24 Å, R_2=40 Å	R_1=27.2 Å, R_2=37.5 Å
15	4.8	Ellipsoid	R_1=24 Å, R_2=50 Å	R_1=27.5 Å, R_2=48.4 Å
15	9.3	Ellipsoid	R_1=24 Å, R_2=95 Å	R_1=25 Å, R_2=86 Å
15	11.1	Ellipsoid	R_1=26 Å, R_2=125 Å	R_1=28.8 Å, R_2=114 Å
15	12.9	Cylinder	R=32 Å, L=400 Å	R=36 Å, L=396 Å
15	14.7	Cylinder	R=32 Å, L=450 Å	R=34 Å, L=450 Å
15	16.4	Cylinder	R=33 Å, L=500 Å	R=36 Å, L=437 Å
15	24.8	Cylinder	R=40 Å, L=600 Å	R=45 Å, L=588 Å

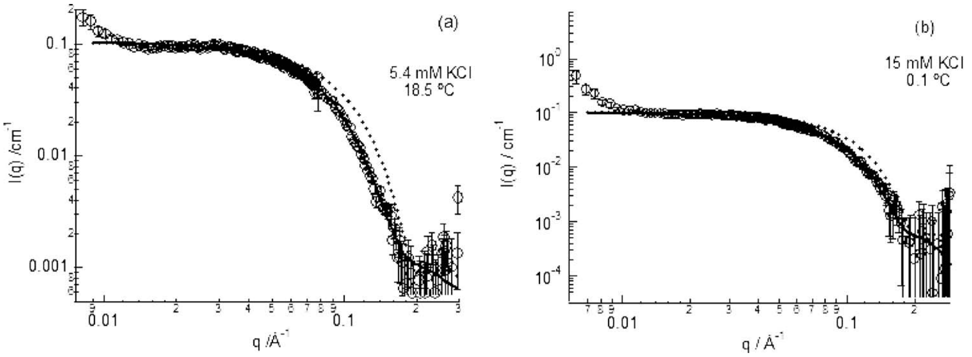

FIG. 4. The SANS data (open circles) for unpolymerized actin showing fits to a polydisperse noninteracting hard-sphere model (solid lines) or to an oblate ellipsoidal model (dotted lines) for (a) 5.4-mM KCl at 18.5 °C and (b) 15-mM KCl at 0.1 °C.

the data at 5.4-mM KCl and 18.5 °C and (b) the fit of the polydisperse hard sphere and the oblate ellipsoid models for the data at 15-mM KCl and 0.1 °C. Figure 4(a) indicates that the actin under these conditions can be described as a sphere with a radius of 23±1 Å and a polydispersity of 18%. Figure 4(b) indicates a sphere of radius of 25±1 Å with a polydispersity of 18% again. As discussed above in the Introduction, x-ray diffraction studies of *G*-actin indicate that the molecule is an oblate ellipsoid with dimensions of 55×55×35 Å. Figures 4(a) and 4(b) also show our attempts to fit the data using oblate ellipsoids as the scattering particles, but those models do not fit the data. The q regimes in which the oblate ellipsoid models deviate from the data are not regimes where the $S(q)$ would contribute to the scattering, so the omission of $S(q)$ does not explain the failure of the oblate ellipsoid as a model scatterer. It should also be noted that the differences between the two fits (sphere and ellipsoid) cannot be explained by polydispersity alone. Similar fits to monodisperse spheres and ellipsoids were performed and the monodisperse sphere showed a better fit to the data. These modeling results for unpolymerized actin in solution indicate the presence of spheres of radius 23–25 Å. The observed polydispersity indicates variation in size and shape, possibly due to the presence of both monomers and dimers under these experimental conditions.[29,30]

Examples of the SANS scattering from actin oligomers modeled as prolate ellipsoids are shown in Fig. 5. Data for 8.9-mM KCl at 4.8 °C are shown in Fig. 5(a) and the fit parameters are R_1(short axis)=22±1 Å and R_2(long axis) =38±1 Å, giving overall dimensions of 44×76 Å. The data and the fit indicate that the actin has just only started to polymerize under these conditions, with some mix of small oligomers, which is in agreement with the results from the scaling of $I(q)$ at low q (see Table I) of $q^{-0.13}$, where the scaling exponent is greater than zero (expected for a sphere) but much less than one (expected for a cylinder). The data in Fig. 5(b), however, are much different: The fitted parameters at 15-mM KCl and 11.1 °C are R_1=26±1 Å and R_2 =125±1 Å. (Fits to other data sets for polymerizing oligomeric actin are shown in Table II.) The parameters suggest that the polymerization of actin is indeed taking place and complement the observation (Table I) of scaling in $I(q)$ of $q^{-0.97}$. Some data points at low q in Figs. 5(a) and 5(b) do not fit to the model and indicate the aggregation effects described above. The high-q discrepancy between data and model is due to the fact that the model assumes a sharp interface between the scatterer and the solvent, which is not true for actin. The ratio of 5:1 of the short axis to the long axis gives overall average oligomer dimensions of about 52 ×250 Å, corresponding to a chain of ten monomers (the monomers are offset from one another in the filament so that each monomer adds 27.4 Å to the length of the filament).

The shape of *F*-actin, once formed, is thought to remain cylindrical with an increase in length along the cylindrical axis as the temperature is increased further. Figure 6 shows examples of modeling the SANS scattering from *F*-actin as a cylindrical scatterer. The fitting parameters for Fig. 6 for (a) actin in 8.9-mM KCl at 18.5 °C are R=31±1 Å and L =500±10 Å and (b) actin in 15-mM KCl at 12.9 °C are R =32±1 Å and L=400±10 Å.

The *F*-actin radii, as determined from these and other fits of the scattering from polymerized actin to a model perfect cylinder (see Table II), range from 31 to 40 Å and thus the diameters range between 62 and 80 Å. The x-ray structure determination of *F*-actin gives a maximum diameter of 90–95 Å.[10] *F*-actin, a helical structure, has two different

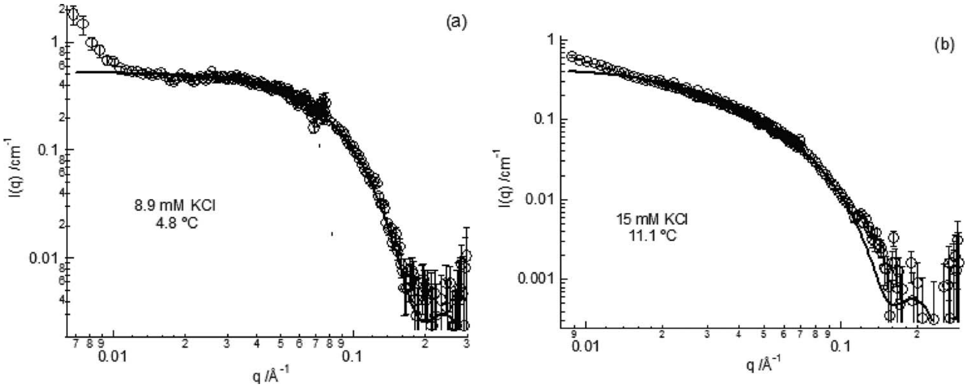

FIG. 5. The SANS data (open circles) for polymerizing actin with fits to a prolate ellipsoid (solid line) for (a) actin with 8.9-mM KCl at 4.8 °C and (b) actin with 15-mM KCl at 11.1 °C.

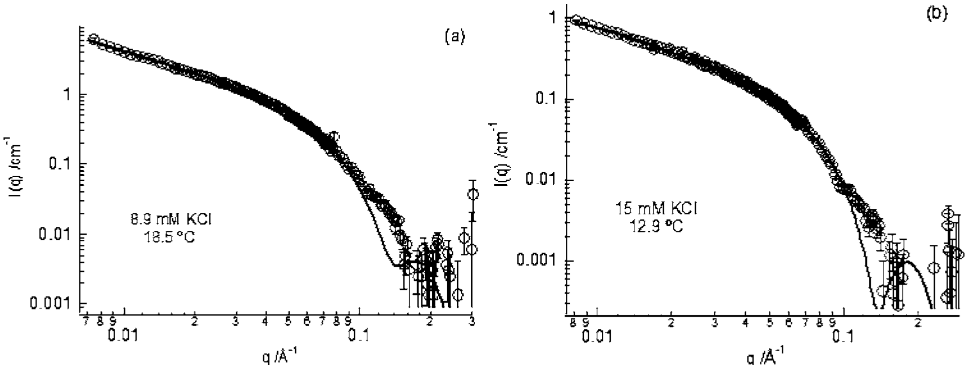

FIG. 6. The SANS data (open circles) for polymerized actin with fits to a cylinder (solid line) for (a) actin with 8.9-mM KCl at 18.5 °C and (b) actin with 15-mM KCl at 12.9 °C.

cross-sectional dimensions: (a) a dimension equivalent to one actin monomer at the minimum diameter of the helix and (b) a dimension equivalent to two actin monomers (a dimer) at the maximum diameter of the helix. In the modeling of the scattering, we are forcing the helix to fit to a cylinder so we should not overinterpret the dimensions obtained from the fits. Indeed, these radii are 2–5 Å lower than what we observe in the $p(r)$ shown in Sec. IV D. The $p(r)$ analysis is model-free and may give more accurate dimensions.

The filament length of F-actin can be up to hundreds of micrometers.[14] The modeling results (Table II) give lengths of 400–700 Å. We believe that these are the full lengths of the filaments formed under these reaction conditions, lengths that correspond to 16–26 monomers. While the extent of polymerization, the fraction of initial monomer that has been incorporated into polymer (Fig. 1), is near one, the degree of polymerization, the average number of monomers in a polymer chain, is small. This means that there are many small oligomeric filaments under the conditions of our experiments.

Figure 7 shows the structural changes that occur when actin is polymerized by heating in KCl solutions.

D. Analysis by generalized indirect Fourier transformation

The $p(r)$ were calculated for the same SANS data that were analyzed by modeling and are shown in Figs. 8–10.[51] Table II shows the parameters obtained from all the $p(r)$ analyses. We note again that we expect the dimensions for the $p(r)$ analysis to be more reliable than those from the modeling.

Figure 8 shows $p(r)$ profiles for unpolymerized G-actin that are typical for a spherical species: The distribution is symmetric about a maximum.[48] The point at which the $p(r)$ falls back to zero is defined as the maximum particle dimension D_{max}.[48] Figure 8(a) indicates that actin at 5.4-mM KCl and 18.5 °C [compare Figs. 3(a) and 4(a)] is a sphere with a most probable particle radius of 27±1 Å and a D_{max} (or particle diameter) of 52±1 Å, in reasonable agreement with the radius determined from SANS modeling (Table II, 23±1 Å). Figure 8(b) shows that actin at 15-mM KCl and 0.1 °C [see Figs. 3(c) and 4(b)] shows even better agreement with the modeling: a spherical particle radius of 25.2±1 Å from $p(r)$ compared to 25±1 Å from the modeling. The "shoulder" in both Figs. 8(a) and 8(b) at ~52±1 Å is probably due to the formation of dimer (17%–23% of the monomer is dimerized under these conditions[30]). To be sure, it can be difficult from the $p(r)$ to distinguish an oblate ellipsoid from a sphere with asymmetry due to polydispersity.[47] However, the scaling exponent of zero and the failure of the modeling as an oblate ellipsoid (see above) both support the interpretation of Fig. 8 as representing spherical monomers in the presence of dimer. In addition, the shoulders in Figs. 8(a) and 8(b) are at the right lengths to represent dimers.[53]

Figures 9(a) and 9(b) show $p(r)$ for polymerizing actin and indicate the initial and latter stages of a prolate ellipsoidal structure, the first being almost spherical and the last being almost a "cylindrical" oligomer. In Fig. 9(a), actin at 8.9-mM KCl and 4.8 °C has a $p(r)$ which is almost symmetrical and closely resembles the $p(r)$ of a sphere. However, on close inspection, the asymmetry at large r values can be seen indicating a very slight elongation of the spherical species. There is a large maximum, which corresponds to the average short axis and is shown at 26±1 Å, in reasonable agreement with the SANS modeling (22±1 Å). However, actin at 15-mM KCl and 11.1 °C [Fig. 9(b)] shows remarkable differences from the $p(r)$ for a sphere. There are two strong maxima and one weak peak between them. The inflection point on the first peak corresponds to the average diameter of the growing polymer of 52 Å,[48,53] to be compared with the SANS modeling (Table II) diameter of 52±2 Å. The weak peak at 150 Å and the strong peak at 225 Å indicate the presence of pentamers and octamers within the polymer chain. The length of the ellipsoid is 250±10 Å, again close to SANS modeling fits of a long axis diameter of 250±20 Å and suggests a total length of nine monomers.

Figure 10 shows $p(r)$ for polymerized actin and the plot corresponds to a cylindrical shape.[48,53] The point of inflection between the first maximum and the (approximately) lin-

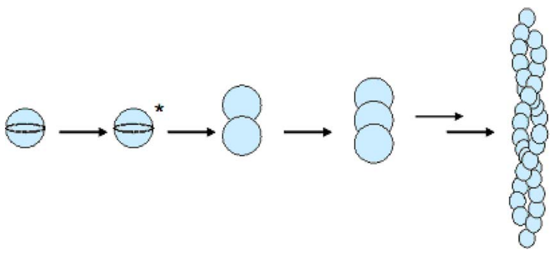

FIG. 7. Schematic showing the structural changes that occur during thermally induced actin protein polymerization in D_2O buffer with KCl as the initiating salt progressing from spherical monomer, to activated spherical monomer (*), to prolate ellipsoid, and to filament.

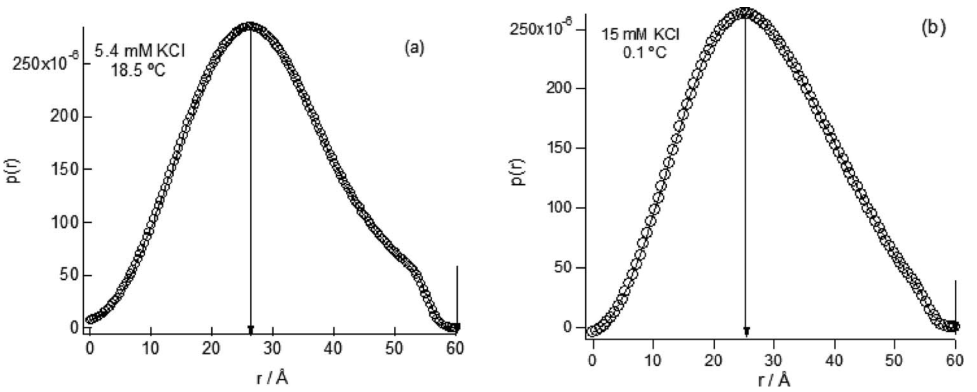

FIG. 8. Pair distance distribution function for unpolymerized actin (a) with 5.4-mM KCl at 18.5 °C and (b) with 15-mM KCl at 0.1 °C. The solid vertical lines indicate the maximum particle cross-sectional diameter and the maximum particle length. Compare Fig. 4.

ear region gives a rough indication for the diameter of the cross section of the cylinder. The cylindrical axis is described by a linear region which decreases to zero, the point at which this occurs is the cylindrical length L. For actin at 8.9-mM KCl and 18.5 °C, a cross-sectional diameter of 75 ± 1 Å and a cylinder length of 495 ± 10 Å are indicated by Fig. 10(a) and listed in Table II. The cross-sectional diameter is thus about 20% larger than that obtained from the SANS modeling ($R = 31 \pm 1$ Å, giving a diameter of 62 ± 2 Å). The length is in close agreement with the length obtained (500 ± 10 Å, Table II) from the modeling. A similar profile is shown in Fig. 10(b) for actin at 15-mM KCl and 12.9 °C. Here the actin has not fully polymerized and thus has a smaller length. The cross-sectional diameter (72 ± 1 Å) is again comparable to that observed from SANS modeling ($R = 32 \pm 1$ Å, diameter $= 64 \pm 2$ Å).

An interesting feature is seen in both cylindrical $p(r)$ profiles in Fig. 10: We would expect a linear region at high q due to the long cylindrical axis. However, in both cases we observe a "rippling" along this region. This effect, we believe, can be attributed to the inhomogeneity along the cylindrical axis. Such an effect has been observed for wormlike micelles of poly(ethylene oxide) block copolymers in aqueous solutions.[54] The rippling is less pronounced in the case of actin, where we attribute the rippling to scattering from the differences in diameter along the actin filament,[53] where each "ripple" corresponds to one monomer unit.

Figure 11 shows the $p(r)$ function for the temperatures investigated at 15-mM KCl. The data at 14.7 °C and the data at 16.4 °C overlay one another; the data at 24.8 °C show considerable scatter and are not plotted. The general trend is that an asymmetry in $p(r)$ becomes apparent as the polymerization process begins. A second maximum is observed as this process continues due to the aggregation of monomers into oligomers. The second peak increases in r and in intensity with increasing temperature, indicating an increased degree of polymerization. On complete polymerization, this second maximum disappears as the structure changes from an ellipsoid to a cylinder. An interesting point to note from the $p(r)$ here is that, contrary to Hansen,[53] for the case of a periodically inhomogeneous rod the magnitude of the peaks of the ripples steadily decreases as r increases, this is not the case for intermediate temperatures. The peaks to the extreme right in these $p(r)$ profiles have almost equal magnitude as the adjacent peaks to their left. This observation was not expected and we currently do not have a firm reasoning for this.

E. Further discussion of actin molecular dimensions

The radii and lengths for the data at 15-mM KCl, as determined by both modeling and GIFT, are plotted in Fig. 12. The dimensions determined from GIFT are more reliable since the GIFT analysis does not impose a model or require a least-squares fit and since modeling does not allow for flexibility or polydispersity. The average radius increases as a function of temperature as the extent of polymerization is increased. This indicates the presence of monomer at low temperatures, dimer at increased temperatures, and filament above the polymerization temperature of about 12 °C. The length of the actin assembly also increases with temperature: There is a steady increase up until the temperature of polymerization at which a rapid increase is observed.

We can compare the actin dimensions from the SANS

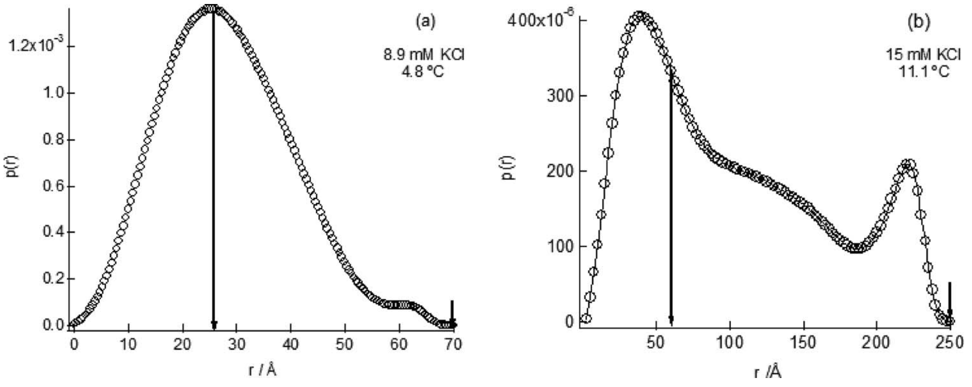

FIG. 9. Pair distance distribution function for polymerizing actin (a) with 8.9-mM KCl at 4.8 °C and (b) with 15-mM KCl at 11.1 °C. The solid vertical lines indicate the maximum particle cross-sectional diameter and the maximum particle length. Compare Fig. 5.

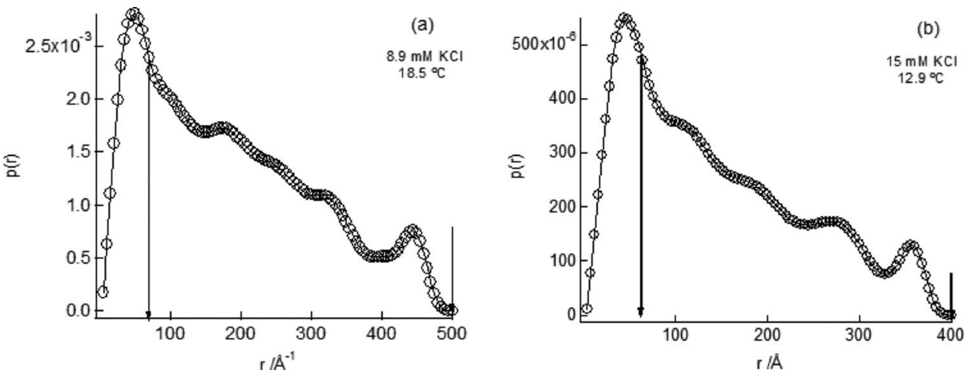

FIG. 10. Pair distance distribution function for polymerized actin (a) with 8.9-mM KCl at 18.5 °C and (b) with 15-mM KCl at 12.9 °C. The solid vertical lines indicate the maximum particle cross-sectional diameter and the maximum particle length. Compare Fig. 6.

analysis in D_2O solution with the structures from x-ray diffraction in actin crystals. The x-ray diffraction studies of monomeric *G*-actin[4–9] indicate that the *G*-actin molecule in a crystal is roughly an *oblate ellipsoid* with dimensions of $55 \times 55 \times 35$ Å. The SANS studies we report here show the unpolymerized actin to be a *spherical* species with a diameter (from the GIFT analysis) of 50–54 Å. There are two interpretations of this result. One is that the species that we see by SANS analysis in solution are entirely dimers rather than monomers and that a dimer is made of two monomers connected on the larger "faces" of the oblate ellipsoids, with some contraction upon connection so that the connection of two 35-Å entities becomes closer to 54 Å than to 70 Å. This interpretation is not consistent with our work showing that only about 20% of the actin is polymerized as dimer below the polymerization temperature (see Fig. 1).[30] The other interpretation of the result is that *G*-actin in solution has a more spherical geometry than it does in a crystal. It would not be surprising to find a different shape in aqueous buffer than in the crystal since the interactions with water and salt are crucial to the polymerization process.[55,56] Moreover, the solution is in D_2O buffer and D_2O has stronger hydrogen bonding and stronger hydrophobic interactions than does H_2O.[30,57] The spherical shape in solution can be due to changes in the conformation of the actin, due to interactions with solvent and salt.

There has been some prior work measuring the dimensions of *G*-actin in solution. One dynamic light-scattering study in H_2O without initiating salt has indicated a sphere of diameter 53 Å (including a hydration layer),[58] and another such study has indicated an ellipsoid of dimensions 84×34 Å.[59] Two x-ray scattering studies in H_2O without initiating salt have indicated a nonspherical shape with a radius of gyration of 24.5 (Ref. 60) or 26 Å.[61] The only other study in D_2O, but without initiating salt, reports only a radius of gyration of 19.9 Å.[62] No other study has been under the same conditions as our study: rabbit muscle actin in D_2O buffer with ATP and KCl as the initiating salt.

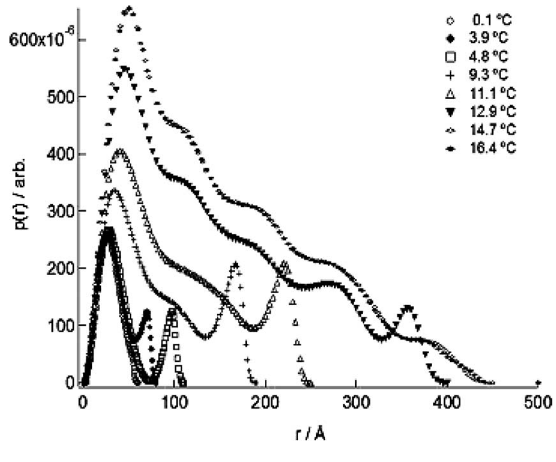

FIG. 11. Pair distance distribution function $p(r)$ for all temperatures of actin polymerization in D_2O buffer at 15-mM KCl.

X-ray diffraction indicates that *F*-actin in a crystal is a double-stranded right-handed helix with a maximum diameter of 90–95 Å (Ref. 10) and a crossover distance of 360 Å, giving a helical turn or pitch of 720 Å.[2] From Table II and Fig. 12, the radii of the *F*-actin filaments from the SANS data are 36 to 45 Å giving average diameters of 72–90 Å, which are consistent with the x-ray analysis if some of the oligomers are not completely formed helices. The GIFT and modeling analyses yield filament lengths that are in the range of 400–700 Å (Table II), we interpret these lengths to be the full contour lengths of the rather small filaments.

V. CONCLUSIONS

A new analysis of small-angle neutron-scattering data from rabbit muscle actin, in the course of the polymerization from *G*-actin to *F*-actin as a function of temperature, yields information regarding the actin sizes and shapes during polymerization in D_2O in the presence of ATP and KCl and with Ca^{2+} as the divalent cation.

Monomeric *G*-actin in D_2O buffer is found to be spherical with a diameter of 50–54 Å with a polydispersity of 15%–20%. The evidence is that the scattering data for *G*-actin cannot be fitted by an oblate ellipsoid model, but can be fitted by a spherical model, and that a spherical shape is consistent with the GIFT analysis. The observed spherical shape of *G*-actin differs from the oblate ellipsoidal shape seen in x-ray structures of actin in crystalline form. The polydispersity indicates fluctuations in the size and shape of the actin monomers and the presence of some dimers. The intermediates between the monomeric and polymeric forms of actin are shown to be prolate ellipsoids that elongate further as temperature and salt concentration are increased. We do not see pair distribution functions that would correspond the "antiparallel" dimers that can occur when the monomers are oblate ellipsoids.[26] The polymeric form of actin is shown,

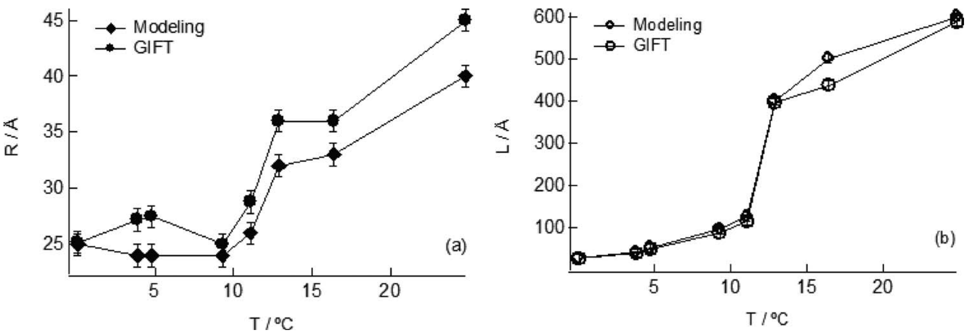

FIG. 12. (a) Radius (filled symbols) and (b) length (open symbols) of actin in 15-mM KCl as a function of temperature determined by SANS modeling (diamonds) and GIFT (circles).

as expected, to adopt a cylindrical conformation of dimensions close to that observed by x-ray diffraction experiments on *F*-actin.

Since the SANS measurements were carried out in D_2O, the shapes and sizes adopted may differ somewhat from the shapes and sizes in H_2O as the solvent because H_2O and D_2O differ in the strengths of hydrogen bonds and of hydrophobic interactions. It would be of interest to repeat this study in H_2O by x-ray scattering, to perform electron microscopy on the actin oligomers, and to study the structure of actin in solution by nuclear magnetic-resonance spectroscopy. These experiments are carried out in the presence of an initiating salt: It will also be of interest to examine the structure of *G*-actin in solution in the absence of an initiating salt.

ACKNOWLEDGMENTS

This research was supported by the National Science Foundation, Chemistry Division. The authors acknowledge the support of the National Institute of Standards and Technology, U. S. Department of Commerce in providing the neutron research facilities used in this work. One of the authors (J.F.) thanks Kuan Wang, Chief of LMB, NIAMS for the encouragement and support of this project. Another author (S.G.) acknowledges the support of the University of Maryland College Park, Division of Research and Graduate Studies.

[1] F. Oosawa and S. Asakura, *Thermodynamics of the Polymerization of Protein* (Academic, New York, 1975).
[2] L. A. Amos and W. B. Amos, *Molecules of the Cytoskeleton* (Guilford, New York, 1991).
[3] P. Sheterline, J. Clayton, and J. C. Sparrow, *Actin*, 4th ed. (Oxford University Press, Oxford, 1998).
[4] W. Kabsch, H. G. Mannherz, D. Suck, E. F. Pai, and K. C. Holmes, Nature (London) **347**, 37 (1990).
[5] P. J. McLaughlin, J. T. Gooch, H.-G. Mannherz, and A. G. Weeds, Nature (London) **364**, 685 (1993).
[6] R. C. Robinson, M. Mejillano, V. P. Le, L. D. Burtnick, H. L. Yin, and S. Choe, Science **286**, 1939 (1999).
[7] W. M. Morton, K. R. Ayscough, and P. J. McLaughlin, Nat. Cell Biol. **2**, 376 (2000).
[8] L. R. Otterbein, P. Graceffa, and R. Dominguez, Science **293**, 708 (2001).
[9] E. M. De La Cruz and T. D. Pollard, Science **293**, 616 (2001).
[10] K. C. Holmes, D. Popp, W. Gebhard, and W. Kabsch, Nature (London) **347**, 44 (1990).
[11] E. H. Egelman and D. J. DeRosier, J. Mol. Biol. **116**, 623 (1983).
[12] E. H. Egelman, N. Francis, and D. J. DeRosier, Nature (London) **298**, 131 (1982).
[13] E. H. Egelman and R. Padron, Nature (London) **307**, 56 (1984).
[14] A. Bremer and U. Aebi, J. Struct. Biol. **119**, 295 (1997).
[15] T. P. Stossel, Am. Sci. **78**, 408 (1990).
[16] T. P. Stossel, Sci. Am. **271**, 54 (1994).
[17] W. Roush, Science **269**, 30 (1995).
[18] D. Pantaloni, C. L. Clainche, and M.-F. Carlier, Science **292**, 1502 (2001).
[19] J. Marx, Science **302**, 214 (2003).
[20] J. A. Cooper, J. E. Loren Buhle, S. B. Walker, T. Y. Tsong, and T. D. Pollard, Biochemistry **22**, 2193 (1983).
[21] T. D. Pollard and J. A. Cooper, Annu. Rev. Biochem. **55**, 987 (1986).
[22] L. A. Selden, H. J. Kinosian, J. E. Estes, and L. C. Gershman, Biochemistry **39**, 64 (2000).
[23] F. Oosawa and M. Kasai, J. Mol. Biol. **4**, 10 (1962).
[24] A. Wegner and J. Engel, Biophys. Chem. **3**, 215 (1975).
[25] R. Millonig, H. Salvo, and U. Aebi, J. Cell Biol. **106**, 785 (1988).
[26] R. Reutzel, C. Yoshioka, L. Govindasamy, E. G. Yarmola, M. Agbandje-Mckenna, M. R. Bubb, and R. McKenna, J. Struct. Biol. **146**, 291 (2004).
[27] R. Ivkov, J. G. Forbes, and S. C. Greer, J. Chem. Phys. **108**, 5599 (1998).
[28] A. P. Andrews, K. P. Andrews, S. C. Greer, F. Boue, and P. Pfeuty, Macromolecules **27**, 3902 (1994).
[29] P. S. Niranjan, J. G. Forbes, S. C. Greer, J. Dudowicz, K. F. Freed, and J. F. Douglas, J. Chem. Phys. **114**, 10573 (2001).
[30] P. S. Niranjan, P. B. Yim, J. G. Forbes, S. C. Greer, J. Dudowicz, K. F. Freed, and J. F. Douglas, J. Chem. Phys. **119**, 4070 (2003).
[31] R. F. Bacon and R. Fanelli, J. Am. Chem. Soc. **65**, 639 (1943).
[32] B. Hammouda, S. Krueger, and C. J. Glinka, J. Res. Natl. Inst. Stand. Technol. **98**, 31 (1993).
[33] J. Lemmich, K. Mortensen, J. H. Ipsen, T. Honger, R. Bauer, and O. G. Mountsen, Phys. Rev. E **53**, 5169 (1996).
[34] See EPAPS Document No. E-JCPSA6-123-517532 for tables of SANS scattering intensity as a function of wave number. This document can be reached via a direct link in the online article's HTML reference section or via the EPAPS homepage (http://www.aip.org/pubservs/epaps.html).
[35] A. Guinier and G. Fournet, *Small-Angle Scattering of X-rays* (Wiley, New York, 1955).
[36] G. Porod, in *Small Angle X-ray Scattering*, edited by O. Glatter and O. Kratky (Academic, London, 1982).
[37] J. S. Higgins and H. C. Benoit, *Polymers and Neutron Scattering* (Clarendon, Oxford, 1994).
[38] G. Beaucage, J. Appl. Crystallogr. **28**, 717 (1995).
[39] http://www.ncnr.nist.gov/resources/sansmodels
[40] J. Hayter, in *Physics of Amphiphile, Micelles, Vesicles, and Microemulsions*, edited by V. DeGiorgio and M. Corti (Elsevier, New York, 1983), p. 69.
[41] W. L. Griffith, R. Triolio, and A. L. Compere, Phys. Rev. A **35**, 2200 (1987).
[42] J. K. Percus and G. J. Yevick, Phys. Rev. **110**, 1 (1958).
[43] O. Glatter, in *Neutrons, X-rays, and Light: Scattering Methods Applied to Soft Condensed Matter*, edited by P. Lindner and T. Zemb (Elsevier, Amsterdam, 2002), pp. 73.
[44] J. Brunner-Popela and O. Glatter, J. Appl. Crystallogr. **30**, 431 (1997).
[45] O. Glatter, J. Appl. Crystallogr. **10**, 415 (1977).
[46] O. Glatter, J. Appl. Crystallogr. **13**, 577 (1980).
[47] O. Glatter, in *Neutron, X-ray, and Light Scattering: Introduction to an Investigative Tool for Colloidal and Polymeric Systems*, edited by P. Lindner and T. Zemb (North-Holland, New York, 1990), pp. 33.
[48] O. Glatter, in *Neutrons, X-rays, and Light: Scattering Methods Applied to Soft Condensed Matter*, edited by P. Lindner and T. Zemb (Elsevier, Amsterdam, 2002), pp. 103.

[49] B. Weyerich, J. Brunner-Popela, and O. Glatter, J. Appl. Crystallogr. **32**, 197 (1999).

[50] J. Brunner-Popela, R. Mittelbach, R. Strey, K. V. Schubert, E. W. Kaler, and O. Glatter, J. Chem. Phys. **110**, 10623 (1999).

[51] O. Glatter, GIFT, University of Graz, Austria, http://physchem.kfunigraz.ac.at/sm/

[52] J. X. Tang and P. A. Janmey, J. Biol. Chem. **271**, 1 (1996).

[53] S. Hansen, J. Appl. Crystallogr. **36**, 1190 (2003).

[54] A. I. Norman, D. L. Ho, A. Karim, and E. J. Amis, J. Colloid Interface Sci. **288**, 155 (2005).

[55] J. Israelachvili and H. Wennerstrom, Nature (London) **379**, 219 (1996).

[56] N. Fuller and R. P. Rand, Biophys. J. **76**, 3261 (1999).

[57] A. Engdahl and B. Nelander, J. Chem. Phys. **86**, 1819 (1987).

[58] J. Masai, S. Ishiwata, and S. Fujime, Biophys. Chem. **25**, 253 (1986).

[59] A. Patkowski, W. Eimer, J. Seils, G. Schneider, B. M. Jockusch, and T. Dorfmueller, Biopolymers **30**, 1281 (1990).

[60] P. Matsudaira, J. Bordas, and M. H. J. Koch, Proc. Natl. Acad. Sci. U.S.A. **84**, 3151 (1987).

[61] Z. Sayers, M. H. J. Koch, J. Bordas, and U. Lindberg, Eur. Biophys. J. **13**, 99 (1985).

[62] D. W. Goddette, E. C. Uberbacher, G. J. Bunick, and C. Frieden, J. Biol. Chem. **261**, 2605 (1986).